Comptes Rendus

Mécanique

Sabrina Bénard, Loic Cappanera, Wietze Herreman and Caroline Nore

Magnetic field based finite element method for magneto-static problems with discontinuous electric potential distributions

The scientific legacy of Roland Glowinski / *L'héritage scientifique de Roland Glowinski*

Magnetic field based finite element method for magneto-static problems with discontinuous electric potential distributions

Sabrina Bénard [a], **Loic Cappanera** [b], **Wietze Herreman** [c] **and Caroline Nore**[*, a]

[a] Université Paris-Saclay, CNRS, LISN, 91400 Orsay, France

[b] Department of Mathematics, University of Houston, Houston, Texas 77204, USA

[c] Université Paris-Saclay, CNRS, FAST, 91400 Orsay, France

E-mails: sabrina.benard@universite-paris-saclay.fr (S. Bénard),
lmcappan@central.uh.edu (L. Cappanera),
wietze.herreman@universite-paris-saclay.fr (W. Herreman),
caroline.nore@universite-paris-saclay.fr (C. Nore)

Abstract. We introduce two finite element formulations to approximate magneto-static problems with discontinuous electric potential based respectively on the electrical scalar potential and the magnetic field. This work is motivated by our interest in Liquid Metal Batteries (LMBs), a promising technology for storing intermittent renewable sources of energy in large scale energy storage devices. LMBs consist of three liquid layers stably stratified and immiscible, with a light liquid metal on top (negative electrode), a molten salt in the middle (electrolyte) and a heavier liquid metal on bottom (positive electrode). Energy is stored in electrical potential differences that can be modeled as jumps at each electrode-electrolyte interface. This paper focuses on introducing new finite element methods for computing current and potential distributions, which account for internal voltage jumps in liquid metal batteries. Two different formulations that use as primary unknowns the electrical potential and magnetic field, respectively, are presented. We validate them using various manufactured test cases, and discuss their applications for simulating the current distribution during the discharge phase in a liquid metal battery.

Keywords. magnetohydrodynamics, finite element methods, interior penalty techniques, discontinuous electric potential, liquid metal batteries.

---

* Corresponding author.

1. Introduction

Magnetohydrodynamics (MHD) is a branch of physics that studies the behavior of electrically conducting fluids, such as liquid metals, in the presence of a magnetic field or an electrical current. MHD is important in various engineering and scientific applications, including power generation, materials processing and energy storage.

The MHD equations consist of the incompressible Navier–Stokes equations coupled to the Maxwell equations in the quasi-static approximation. In the incompressible Navier–Stokes equations, a major challenge for mathematicians and physicists is that the pressure and velocity are coupled via the incompressiblity constraint. This led to the development of operator splitting methods [1–4], and more generally to numerical approximation methods for non-linear variational problems [5], that allow to decouple and approximate these equations. For instance, a popular way to approximate incompressible Navier–Stokes equations is to use projection methods where the problem is decoupled into a sequence of parabolic and elliptic equations for the velocity and pressure, respectively. We refer to [6] for an overview of projection methods.

One of the promising applications of MHD is in liquid metal batteries (LMBs), which are a novel type of energy storage system with potential use in grid-scale energy storage for renewable energy sources. These sources, such as wind and sunlight, are by essence highly intermittent, however they will play a crucial role in electricity generation in near future if they can be stored at low cost. Liquid metal batteries consist of two layers of liquid metals of different densities, separated by a thin layer of electrolyte. They are concentration cells where electrochemical reactions affect the composition of the liquid metal electrodes [7]. The cell voltage is generated by variations of the partial molar Gibbs free energy of the electroactive component that is exchanged between the negative (top layer) and the positive electrode (bottom layer). In other words, energy is stored in these batteries by alloying and de-alloying processes in the liquid metal electrodes. LMBs can be described as electrochemical cells with sharp interfaces between the electrodes and electrolyte. Other cells, such as alkaline electrolyzers, molten salt batteries, and aluminum reduction cells, are widely used in various industrial applications. In these systems, an electrode is in contact with an electrolyte, creating a sharp interface where electrochemical reactions take place. This interface is critical for the overall performance of the cell, as it determines the rate and efficiency of the electrochemical processes. It can be modelled by a macroscopic approach where the continuous change of electric potential over the electrical double layer is replaced by a discrete jump in electrical potential (see [8] and references therein). This approach has been recently used in a Finite Volume Method (FVM) model coupled with a microscopic description of potential difference and different overpotentials in the electrolyte and the electrodes that influence the cell voltage of a battery [9]. It is extremely valuable in that it allows not only to model electrochemical cells up to the meter scale, but also to take into account all the spatial variations of overvoltages and the three-dimensional distribution of current and potential. Overviews of numerical methods used for the modeling of the current and electrical potential distributions in LMBs can be found in [10, 11].

The objective of this article is twofold: we intend to use the mentioned macroscopic approach to model the discontinuous electric potential distributions between an electrode and an electrolyte using two different formulations, one based on a formulation with the electrical potential directly (as done in [8, 9, 12]) and a new one based on the magnetic field. The transmission problem on the electrode-electrolyte interfaces is represented by interface jump conditions on the electrical potential and the curl of the magnetic field divided by the electrical conductivity, respectively, and is enforced via the use of interior penalty Galerkin methods. These transmission conditions are related to conditions imposed between solid parts and fluid in fluid-structure problems as developed in the work of Prof. Roland Glowisnki and co-authors in [13].

The paper is organized as follows. In Section 2, we present a formulation using the electrical potential and check its convergence with manufactured solutions. In Section 3, we introduce a novel formulation that uses the magnetic field as primary unknown. We show the equivalency between both formulations by comparing both methods on various setups in Section 4. We conclude in Section 5.

2. Formulation problem with electric potential φ

We first present a model for discontinuous electrical potential distributions between an electrolyte and an electrode.

2.1. *Problem description*

Let us consider a domain $\Omega \subset \mathbb{R}^3$ with boundary $\Gamma = \partial\Omega$. The domain is assumed to be partitioned in two subdomains Ω_1 and Ω_2 such that $\overline{\Omega} = \overline{\Omega_1} \cup \overline{\Omega_2}$, $\Omega_1 \cap \Omega_2 = \emptyset$. The interface between both domains is denoted by $\Sigma = \overline{\Omega_1} \cap \overline{\Omega_2}$. We denote by φ the electric potential and by σ the electrical conductivity. We denote by $\varphi_1, \sigma_1, \varphi_2, \sigma_2$ their restrictions to the subdomain Ω_1 and Ω_2, respectively. A sketch of the domain is displayed in Figure 1.
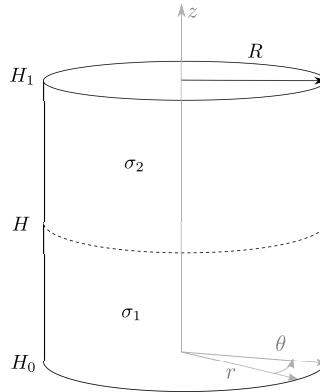

Figure 1. Cylindrical domain used for numerical investigations: electrolyte on top, electrode on bottom.

Using the electric potential φ as primary unknown, the magneto-static equation can be written as the following elliptic equation:

$$-\nabla \cdot (\sigma \nabla \varphi) = 0 \qquad \text{in } \Omega_1 \text{ and } \Omega_2, \tag{1a}$$

$$\varphi_1 - \varphi_2 = \varphi_{\text{jump}} \qquad \text{on } \Sigma, \tag{1b}$$

$$(\sigma_1 \nabla \varphi_1 - \sigma_2 \nabla \varphi_2) \cdot \boldsymbol{n} = 0 \qquad \text{on } \Sigma, \tag{1c}$$

where φ_{jump} is a given function that represents the jump of electrical potential at the interface Σ and $\boldsymbol{n}$ the outward normal to the surface Σ. We note that these equations are also supplemented with either Dirichlet or homogeneous Neumann boundary conditions.

2.2. *Space discretization*

In the sequel, we use cylindrical coordinates (r, θ, z) as indicated in Figure 1. We assume that the domain Ω is axisymmetric which allows us to use a Fourier decomposition in the azimuthal direction θ as it is done in the SFEMaNS code used to perform all the numerical simulations reported in this paper. The Fourier components of the electric potential can then be approximated on a meridian section Ω^{2D} of the domain Ω using finite elements. We refer to [14–16] for more information on the SFEMaNS code

It leads us to introduce a regular family of non-overlapping quadratic triangle meshes that we denote by $(\mathcal{E}_h)_{h>0}$ and the meridian finite element space:

$$X_h^{2D} = \left\{ v \in L^2\left(\Omega^{2D}\right); v_{|\Omega_i^{2D}} \in C^0\left(\overline{\Omega_i^{2D}}\right), \quad \text{for } i = 1, 2; v(T_K)_{|K} \in \mathbb{P}_2, \forall\, K \in \mathcal{E}_h \right\},$$

where h represents the mesh size (i.e the diameter of cells K) and T_K represents the quadratic transformation that maps the reference element $\widehat{K} = \{(r, z); 0 \le r, 0 \le z, r^2 + z^2 \le 1\}$ to the element K of $\mathcal{E}_h$. The electric potential is then approximated in the following space:

$$X_h = \left\{ \varphi = \sum_{m=-M}^{M} \varphi_h^m(r, z) e^{im\theta}; \varphi_h^m \in X_h^{2D}, \overline{\varphi_h^m} = \varphi_h^{-m}, \forall\, m \in \overline{0, M} \right\},$$

where $M + 1$ represents the maximum number of complex Fourier modes used in the Fourier decomposition. The meridian section of the interface Σ is represented by a family of quadratic triangular finite elements Σ_h^{2D}. For each element F in Σ_h^{2D}, we denote by h_F the local mesh size, i.e. the diameter of the triangle F.

To avoid excessive notation when introducing the weak formulation of our problems, the following assumes that no Fourier decomposition is used, that the unknown φ lives in a three dimensional finite element space also denoted by X_h and that elements live on a space denoted by Σ_h.

2.3. *Weak Formulation*

The discrete problem for the electric potential reads: find $\varphi \in X_h$ such that the following holds for all $\psi \in X_h$

$$\int_{\Omega_1} \sigma \nabla\varphi \cdot \nabla\psi\, dV + \int_{\Omega_2} \sigma \nabla\varphi \cdot \nabla\psi\, dV - \int_{\Sigma} \left(\rho_1 \sigma_1 \nabla\varphi_1 \cdot \boldsymbol{n_1} - \rho_2 \sigma_2 \nabla\varphi_2 \cdot \boldsymbol{n_2}\right) (\psi_1 - \psi_2)\, dS$$

$$+ \beta \int_{\Sigma} \Lambda h_F^{-1}(\varphi_1 - \varphi_2)(\psi_1 - \psi_2)\, dS = \beta \int_{\Sigma} \Lambda h_F^{-1} \varphi_{\text{jump}}(\psi_1 - \psi_2)\, dS, \quad (2)$$

where the boundary conditions (Dirichlet or Neumann) are enforced strongly. For Dirichlet conditions, we set φ equal to a given boundary condition g on $\partial\Omega$. Neumann boundary conditions are enforced similarly. The harmonic average Λ and weight ρ_i are defined by:

$$\Lambda = \frac{2\sigma_1 \sigma_2}{\sigma_1 + \sigma_2}, \quad \rho_1 = \frac{\sigma_2}{\sigma_1 + \sigma_2}, \quad \rho_2 = \frac{\sigma_1}{\sigma_1 + \sigma_2}. \quad (3)$$

We refer to the work of [17] for more information on the origin of these average and weight formulas. The constant β represents a tunable penalty parameter that is always set to one in our numerical investigations. The vector $\boldsymbol{n_i}$ is the outward normal vector to the interface Σ with respect to Ω_i. We note that, unlike the interface condition (1b) that is enforced weakly, meaning that it is enforced in the weak formulation (2) using the terms in the second line, the interface condition (1c) is enforced strongly like the boundary conditions.

2.4. *Numerical investigations*

In this section, we run two sets of tests using manufactured solutions to ensure the good behavior of the SFEMaNS code when solving the above weak formulation. First, a series of tests with $\varphi_{\text{jump}} = 0$ is performed, then, another series of tests is done with a given jump in electric potential around the interface Σ. All tests are performed on the domain $\Omega = \{(r, \theta, z); 0 \le r \le R, 0 \le \theta < 2\pi, H_0 \le z \le H_1\}$ with the interface $\Sigma = \{(r, \theta, z) \in \Omega; z = H\}$ where we set $R = 0.5, H_0 = 0, H_1 = 1, H = 0.5$.

The manufactured solutions used in this section are determined using the method of separation of variables. They involve the first kind Bessel functions denoted by J_m and the n$^{\text{th}}$ root of J'_m denoted by κ'_{mn}. In the following, our numerical tests involve the roots $\kappa'_{01}, \kappa'_{11}$ and κ'_{21} whose approximate values are reported below for completeness:

$$\kappa'_{01} = 3.8317059702, \quad \kappa'_{11} = 1.841183781200789, \quad \kappa'_{21} = 3.054236935206724.$$

2.4.1. *Tests with $\varphi_{\text{jump}} = 0$ and $\sigma = 1$*

We consider three sets of tests that involve the Fourier mode $m = 0, 1, 2$. The electrical conductivity σ is set to one in the whole domain. The manufactured solutions are defined as follows:

- **Test 1** (mode $m = 0$):
  $\varphi(r, z) = J_0(kr) \, \sinh(k(z + H_0))$ with $k = \kappa'_{01}/R$.
- **Test 2** (mode $m = 1$):
  $\varphi(r, z, \theta) = e^{i\theta} J_1(kr) \sinh(k(z + H_0))$ with $k = \kappa'_{11}/R$.
- **Test 3** (mode $m = 2$):
  $\varphi(r, z, \theta) = e^{2i\theta} J_2(kr) \cosh(k(z - H_1))$ with $k = \kappa'_{21}/R$.
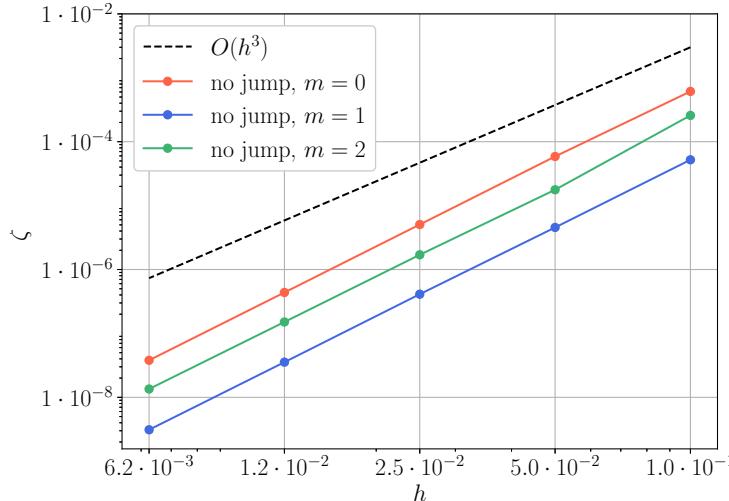
Figure 2. Order of convergence of L^2 relative errors in electric potential when $\varphi_{\text{jump}} = 0$ with respect to mesh size h. The dash line represents the theoretical order of convergence h^3.

We note that a homogeneous Neumann boundary condition is applied on the lateral face of the domain ($r = R$) and that Dirichlet boundary conditions are applied on the lids of the cylinder ($z = H_0$ and $z = H_1$). We denote by ζ the relative errors in L^2-norm of the electric potential defined by

$$\zeta_\varphi = \frac{\|\varphi_{\text{num}} - \varphi\|_2}{\|\varphi\|_2}, \tag{4}$$

where φ is the exact solution given by the manufactured solutions above and φ_{num} the numerical approximation. The relative errors with respect to the non-dimensionalised mesh size h are reported in Table 2. We recover the theoretical order of convergence, equal to three as we are using quadratic finite elements, as shown in Figure 2.

Table 1. Relative errors in L^2-norm of φ with $\varphi_{\text{jump}} = 0$. The non-dimensionalised mesh size is denoted by h and the number of degrees of freedom by n_{dof}.

h	n_{dof}	$m = 0$	$m = 1$	$m = 2$
0.1	322	$6.12 \cdot 10^{-4}$	$5.21 \cdot 10^{-5}$	$2.58 \cdot 10^{-4}$
0.05	1034	$5.87 \cdot 10^{-5}$	$4.55 \cdot 10^{-6}$	$1.77 \cdot 10^{-5}$
0.025	3886	$5.06 \cdot 10^{-6}$	$4.11 \cdot 10^{-7}$	$1.70 \cdot 10^{-6}$
0.0125	15098	$4.37 \cdot 10^{-7}$	$3.55 \cdot 10^{-8}$	$1.51 \cdot 10^{-7}$
0.00625	59746	$3.80 \cdot 10^{-8}$	$3.11 \cdot 10^{-9}$	$1.35 \cdot 10^{-8}$

2.4.2. *Tests with $\varphi_{\text{jump}} \neq 0$*

In this section we now consider setups with a given jump of the electric potential around the interface Σ that either involve the Fourier mode $m = 0$, $m = 1$, or $m = 2$. The electrical conductivity of the domains Ω_1 and Ω_2 is set to $\sigma_1 = 10^4$ and $\sigma_2 = 1$, respectively. We define the manufactured solutions as follows:

- **Test 1** (mode $m = 0$):

$$\varphi_1(r, z) = J_0(kr) \sinh(k(z + H_0)), z \leq H,$$
$$\varphi_2(r, z) = J_0(kr)\sigma_1/\sigma_2 \sinh(k(z + H_0)), z > H,$$
$$\text{with } k = \kappa'_{01}/R \text{ and } \varphi_{\text{jump}} = J_0(kr)(\sigma_1/\sigma_2 - 1)\sinh(k(H + H_0)).$$

- **Test 2** (mode $m = 1$):

$$\varphi_1(r, z, \theta) = e^{i\theta} J_1(kr) \sinh(k(z + H_0)), z \leq H,$$
$$\varphi_2(r, z, \theta) = e^{i\theta} J_1(kr)\sigma_1/\sigma_2 \sinh(k(z + H_0)), z > H,$$
$$\text{with } k = \kappa'_{11}/R \text{ and } \varphi_{\text{jump}} = e^{i\theta} J_1(kr)(\sigma_1/\sigma_2 - 1)\sinh(k(H + H_0)).$$

- **Test 3** (mode $m = 2$):

$$\varphi_1(r, z, \theta) = e^{2i\theta} J_2(kr) \cosh(k(z - H_1)), z \leq H,$$
$$\varphi_2(r, z, \theta) = e^{2i\theta} J_2(kr)\sigma_1/\sigma_2 \cosh(k(z - H_1)), z > H,$$
$$\text{with } k = \kappa'_{21}/R \text{ and } \varphi_{\text{jump}} = e^{2i\theta} J_2(kr)(\sigma_1/\sigma_2 - 1)\cosh(k(H - H_1)).$$

We note that all the above manufactured solutions satisfy the natural interface condition $\sigma_1 \frac{\partial \varphi_1}{\partial z}|_{z=H} = \sigma_2 \frac{\partial \varphi_2}{\partial z}|_{z=H}$ that corresponds physically to the continuity of the normal component of the electrical current density. As in the previous section, we impose a homogeneous Neumann boundary condition on the lateral face of the cylinder and Dirichlet boundary conditions on the lids. Table 2 displays the relative error in L^2-norm of the electric potential φ. As shown in Figure 3, we recover the theoretical order of convergence in $\mathcal{O}(h^3)$ with h the mesh size.

3. Novel formulation with magnetic field H

We present a novel formulation for magneto-static problems with discontinuous electrical potential using the magnetic field as primary unknown.

Table 2. Relative errors in L^2-norm of φ with $\varphi_{\text{jump}} \neq 0$. The non-dimensionalised mesh size is denoted by h and the number of degrees of freedom by n_{dof}.

| h	n_{dof}	$m = 0$	$m = 1$	$m = 2$
0.1	322	$6.48 \cdot 10^{-4}$	$2.30 \cdot 10^{-4}$	$4.77 \cdot 10^{-3}$
0.05	1034	$7.38 \cdot 10^{-5}$	$3.46 \cdot 10^{-5}$	$7.21 \cdot 10^{-4}$
0.025	3886	$8.14 \cdot 10^{-6}$	$4.70 \cdot 10^{-6}$	$1.10 \cdot 10^{-4}$
0.0125	15098	$8.92 \cdot 10^{-7}$	$5.95 \cdot 10^{-7}$	$1.47 \cdot 10^{-5}$
0.00625	59746	$1.05 \cdot 10^{-7}$	$7.57 \cdot 10^{-8}$	$1.92 \cdot 10^{-6}$
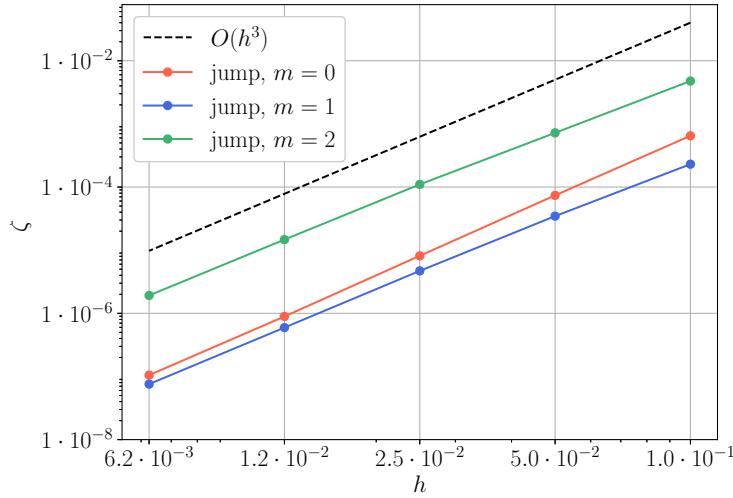
Figure 3. Order of convergence of L^2 relative errors in electric potential when $\varphi_{\text{jump}} \neq 0$ with respect to mesh size h. The dash line represents the theoretical order of convergence h^3.

3.1. *Problem description*

We consider the same problem introduced in Section 2.1. Introducing the electrical current $\mathbf{j} = -\sigma \nabla \varphi$, we note that $\nabla \times (\frac{1}{\sigma} \mathbf{j}) = 0$. As the magnetic field $\mathbf{H}$ satisfies $\nabla \times \mathbf{H} = \mathbf{j}$, we get $\nabla \times (\frac{1}{\sigma} \nabla \times \mathbf{H}) = 0$ inside Ω. Thus, when the electrical potential is continuous across the interface Σ, i.e $\varphi_{\text{jump}} = 0$, we get the following classic equations for the magnetic field:

$$\begin{cases} \nabla \times \left(\dfrac{\nabla \times \mathbf{H}}{\sigma} \right) = 0 & \text{in } \Omega_1 \text{ and } \Omega_2, \\ \nabla \cdot (\mu \mathbf{H}) = 0 & \text{in } \Omega_1 \text{ and } \Omega_2, \end{cases} \tag{5}$$

where μ is the magnetic permeability, set to a constant in the rest of the paper.

To extend this formulation to problems with discontinuous electrical potential across the interface Σ, we note that multiplying the first equation of (5) by a test function $\boldsymbol{v}$ and integrating by part on a domain D reads

$$\int_D \left(\frac{\nabla \times \mathbf{H}}{\sigma} \right) \cdot (\nabla \times \boldsymbol{v}) dV + \int_{\partial D} \left(\left(\frac{\nabla \times \mathbf{H}}{\sigma} \right) \times \boldsymbol{v} \right) \cdot \boldsymbol{n} dS = 0,$$

where $\boldsymbol{n}$ represents the outward normal vector to ∂D.

Using the relation

$$\left(\left(\frac{\nabla \times \mathbf{H}}{\sigma} \right) \times \boldsymbol{v} \right) \cdot \boldsymbol{n} = \left(\boldsymbol{n} \times \left(\frac{\nabla \times \mathbf{H}}{\sigma} \right) \right) \cdot \boldsymbol{v},$$

and the definitions of the electrical current on each side of the interface Σ

$$\boldsymbol{j}_1 \times \boldsymbol{n} = -\sigma_1 \nabla_t \varphi_1 \times \boldsymbol{n}, \qquad \boldsymbol{j}_2 \times \boldsymbol{n} = -\sigma_2 \nabla_t \varphi_2 \times \boldsymbol{n} \quad \text{on } \Sigma,$$

where ∇_t represents the tangential gradient on the interface Σ, we induce that the jump in electrical potential can be translated into a jump on $\frac{\nabla \times \mathbf{H}}{\sigma} \times \boldsymbol{n}$. Indeed, since the magnetic field satisfies $\nabla \times \mathbf{H} = \boldsymbol{j}$, we get:

$$\left(\frac{\nabla \times \mathbf{H}_1}{\sigma_1} - \frac{\nabla \times \mathbf{H}_2}{\sigma_2} \right) \times \boldsymbol{n} = -\nabla_t (\varphi_1 - \varphi_2) \times \boldsymbol{n} \qquad \text{on } \Sigma.$$

Therefore, we propose the following novel formulation in magnetic field:

$$\nabla \times \left(\frac{\nabla \times \mathbf{H}}{\sigma} \right) = 0 \qquad \text{in } \Omega_1 \text{ and } \Omega_2, \tag{6a}$$

$$\nabla \cdot (\mu \mathbf{H}) = 0 \qquad \text{in } \Omega_1 \text{ and } \Omega_2, \tag{6b}$$

$$\left(\frac{\nabla \times \mathbf{H}_1}{\sigma_1} - \frac{\nabla \times \mathbf{H}_2}{\sigma_2} \right) \times \boldsymbol{n} = -(\nabla_t \varphi_{\text{jump}}) \times \boldsymbol{n} \qquad \text{on } \Sigma, \tag{6c}$$

$$(\mathbf{H}_1 - \mathbf{H}_2) \times \boldsymbol{n} = 0 \qquad \text{on } \Sigma, \tag{6d}$$

$$\mu(\mathbf{H}_1 - \mathbf{H}_2) \cdot \boldsymbol{n} = 0 \qquad \text{on } \Sigma. \tag{6e}$$

We note that the last two conditions take into account the continuity of the tangential components of $\mathbf{H}$ and the continuity of the normal component of $\mu\mathbf{H}$, respectively. In the rest of the paper, we will replace the notation $-\nabla_t \varphi_{\text{jump}}$ by $(\frac{\nabla \times \mathbf{H}}{\sigma})_{\text{jump}}$.

Remark 1. Using the Helmholtz decomposition, we recall that the magnetic field $\mathbf{H}$ (vanishing at $\mathbf{r} \to \infty$) is uniquely defined from its curl and divergence (if they are sufficiently smooth and if they vanish faster than $1/|\mathbf{r}|^2$ at infinity) which read:

$$\nabla \times \mathbf{H} = \boldsymbol{j} \quad \text{in } \Omega_1 \text{ and } \Omega_2, \tag{7a}$$

$$\nabla \cdot (\mu \mathbf{H}) = 0 \quad \text{in } \Omega_1 \text{ and } \Omega_2. \tag{7b}$$

In magnetostatics, the electrical current $\mathbf{j}$ can be obtained from the electrical potential φ, solution of the system (1), using the relation

$$\mathbf{j} = -\sigma \nabla \varphi. \tag{8}$$

We note that equation (6a) can be derived from equations (7a) and (8). Similarly, the interface conditions (6c)-(6e) can be derived using equations (7) and (1c). Thus, both formulations (1) and (6) generate the same electrical current $\mathbf{j}$.

3.2. *Weak formulation with* $\mathbf{H}$

We extend the notation introduced in Section 2.2 to vector valued space functions that we denote by $\mathbf{X}_h^{2D}$ and $\mathbf{X}_h$. Unlike the weak formulation of the electrical potential, the weak formulation for the magnetic field needs to account for the continuity of $\mathbf{H} \times \boldsymbol{n}$ and $\mu\mathbf{H} \cdot \boldsymbol{n}$ across the interface Σ. This can be done by adding, in the weak formulation, penalty terms of the form:

$$\beta \int_\Sigma \frac{1}{h} (\mathbf{H}_1 \times \boldsymbol{n}_1 + \mathbf{H}_2 \times \boldsymbol{n}_2) \cdot (\boldsymbol{v}_1 \times \boldsymbol{n}_1 + \boldsymbol{v}_2 \times \boldsymbol{n}_2) \, dS$$

and

$$\beta \int_\Sigma \frac{1}{h} \left(\mu\mathbf{H}_1 \cdot \boldsymbol{n}_1 + \mu\mathbf{H}_2 \cdot \boldsymbol{n}_2 \right) \left(\mu\boldsymbol{v}_1 \cdot \boldsymbol{n}_1 + \mu\boldsymbol{v}_2 \cdot \boldsymbol{n}_2 \right) dS$$

where $\boldsymbol{v}$ represents a test function in $\mathbf{X}_h$ and β a penalty parameter. The weak formulation also needs to enforce the zero divergence condition of the magnetic field. We recall that the space of approximation $\mathbf{X}_h$ uses $\mathbf{H}^1$ conforming finite elements, thus the divergence cannot be approximated in L^2 if the domain Ω is non-smooth or non-convex, see [18]. To overcome

this obstacle, a method based on the work of [19–21] has been implemented in the SFEMaNS code. The method consists of controlling the divergence of $\mathbf{H}$ in a negative Sobolev space H^{-s} with $s \in (0.5, 1)$ on each sub-domain Ω_i by introducing a magnetic pressure p_m solution of the following equation:

$$-\nabla \cdot \left(h^{2(1-\alpha)} \nabla p_m \right) = -\nabla \cdot (\mu \mathbf{H}) \quad \text{in } \Omega_1 \text{ and } \Omega_2, \tag{9}$$

where $\alpha = 1 - s$. Moreover, the above problem is supplemented with homogeneous Dirichlet boundary conditions.

The discrete problem for the magnetic field reads as follows. Find $(\mathbf{H}, p_m) \in \mathbf{X}_h \times X_h$ such that the following holds for all $(\boldsymbol{v}, q) \in \mathbf{X}_h \times X_h$:

$$\int_{\Omega_1} \left(\frac{\nabla \times \mathbf{H}}{\sigma} \right) \cdot (\nabla \times \boldsymbol{v}) dV + \int_{\Omega_2} \left(\frac{\nabla \times \mathbf{H}}{\sigma} \right) \cdot (\nabla \times \boldsymbol{v}) dV + \int_{\Sigma} \left(\theta_1 \frac{\nabla \times \mathbf{H}_1}{\sigma_1} + \theta_2 \frac{\nabla \times \mathbf{H}_2}{\sigma_2} \right) \cdot (\boldsymbol{v}_1 \times \boldsymbol{n}_1 + \boldsymbol{v}_2 \times \boldsymbol{n}_2) dS$$

$$+ \beta_1 \left(\int_{\Omega_1} \mu \nabla p_m \cdot \boldsymbol{v} dV - \int_{\Omega_1} \mu \mathbf{H} \cdot \nabla q dV + \int_{\Omega_1} h^{2(1-\alpha)} \nabla p_m \cdot \nabla q dV + \int_{\Omega_1} h^{2\alpha} \nabla \cdot (\mu \mathbf{H}) \nabla \cdot (\mu \boldsymbol{v}) dV \right)$$

$$+ \beta_1 \left(\int_{\Omega_2} \mu \nabla p_m \cdot \boldsymbol{v} dV - \int_{\Omega_2} \mu \mathbf{H} \cdot \nabla q dV + \int_{\Omega_2} h^{2(1-\alpha)} \nabla p_m \cdot \nabla q dV + \int_{\Omega_2} h^{2\alpha} \nabla \cdot (\mu \mathbf{H}) \nabla \cdot (\mu \boldsymbol{v}) dV \right)$$

$$+ \beta_3 \int_{\Sigma} \frac{1}{h} (\mathbf{H}_1 \times \boldsymbol{n}_1 + \mathbf{H}_2 \times \boldsymbol{n}_2) \cdot (\boldsymbol{v}_1 \times \boldsymbol{n}_1 + \boldsymbol{v}_2 \times \boldsymbol{n}_2) dS$$

$$+ \beta_1 \int_{\Sigma} \frac{1}{h} (\mu \mathbf{H}_1 \cdot \boldsymbol{n}_1 + \mu \mathbf{H}_2 \cdot \boldsymbol{n}_2)(\mu \boldsymbol{v}_1 \cdot \boldsymbol{n}_1 + \mu \boldsymbol{v}_2 \cdot \boldsymbol{n}_2) dS$$

$$+ \int_{\Gamma} \frac{1}{\sigma} (\nabla \times \mathbf{H}) \cdot (\boldsymbol{v} \times \boldsymbol{n}) dS + \beta_3 \int_{\Gamma} h^{-1} (\mathbf{H} \times \boldsymbol{n}) \cdot (\boldsymbol{v} \times \boldsymbol{n}) dS$$

$$= - \int_{\Sigma} \left(\frac{\nabla \times \mathbf{H}}{\sigma} \right)_{\text{jump}} \cdot (\theta_2 \boldsymbol{v}_1 \times \boldsymbol{n}_1 - \theta_1 \boldsymbol{v}_2 \times \boldsymbol{n}_2) dS + \beta_3 \int_{\Gamma} h^{-1} \left(\mathbf{H}_{\text{bdy}} \times \boldsymbol{n} \right) \cdot (\boldsymbol{v} \times \boldsymbol{n}) dS, \tag{10}$$

where the coefficients β_1 and β_3 represent penalty parameters that are set to one. The weights θ_1, θ_2 are defined as follows:

$$\theta_1 = \frac{\sigma_1}{\sigma_1 + \sigma_2}, \quad \theta_2 = \frac{\sigma_2}{\sigma_1 + \sigma_2}.$$

We note that Dirichlet boundary conditions on $\mathbf{H} \times \mathbf{n}$ are enforced weakly using the last term of the left and right hand side (see the two last lines of above weak formulation). Moreover, the interface conditions (6d)-(6e) are also enforced weakly while the condition (6c) is enforced strongly.

3.3. *Numerical investigations*

This section investigates the convergence of the algorithm (10) using manufactured solutions. We consider two main setups that either involve a continuous electric current or an electric current with discontinuous tangential components across the interface Σ. All the tests reported here are performed with Dirichlet boundary conditions on $\partial \Omega$. Moreover, the tests are all performed on the same cylindrical domain Ω considered in section Section 2.4, meaning that $\Omega = \{(r, \theta, z); 0 \leq r \leq R, 0 \leq \theta < 2\pi, H_0 \leq z \leq H_1\}$ with the interface $\Sigma = \{(r, \theta, z) \in \Omega; z = H\}$ where we set $R = 0.5, H_0 = 0, H_1 = 1, H = 0.5$. We choose $\mu = 1$ unless otherwise specified.

In the following we denote by κ_{mn} the nth root of the Bessel function J_m. The numerical tests presented in this section use the roots κ_{11} and κ_{21} whose approximate values are reported below:

$$\kappa_{01} = 2.4048255577, \quad \kappa_{11} = 3.8317059702, \quad \kappa_{21} = 5.1356223018.$$

3.3.1. *Test 1: no jump in* $(\frac{\nabla \times \mathbf{H}}{\sigma}) \times \mathbf{n}$ *with* $\sigma = 1$

Using the separation of variables method, we manufactured a solution **H** of the problem (6), with $\varphi_{\text{jump}} = 0$, defined by

$$H_r = \frac{A J_{m+1}(kr) + B J_{m-1}(kr)}{2} e^{kz} \cos(m\theta), \tag{11a}$$

$$H_\theta = \frac{A J_{m+1}(kr) - B J_{m-1}(kr)}{2} e^{kz} \sin(m\theta), \tag{11b}$$

$$H_z = \frac{A - B}{2} J_m(kr) e^{kz} \cos(m\theta), \tag{11c}$$

where A and B are real constants. In the following, we set $A = 2$, $B = 1$. We note that the above magnetic field is continuous so, when $\sigma = 1$, the continuity of $(\frac{\nabla \times \mathbf{H}}{\sigma}) \times \mathbf{n}$ is naturally enforced. We perform three sets of tests that either use the Fourier mode $m = 0$ and the root $k = \kappa_{01}/R$, the Fourier mode $m = 1$ and the root $k = \kappa_{11}/R$ or the Fourier mode $m = 2$ and the root $k = \kappa_{21}/R$. We denote by ζ the relative errors in $\mathbf{L}^2$-norm of the magnetic field defined by

$$\zeta_{\mathbf{H}} = \frac{\|\mathbf{H}_{\text{num}} - \mathbf{H}\|_2}{\|\mathbf{H}\|_2},$$

where **H** is the exact solution defined in (11a)-(11c) and $\mathbf{H}_{\text{num}}$ the numerical approximation. The relative errors with respect to the non-dimensionalised mesh size are displayed in Table 3. The theoretical order of convergence, equal to three, is recovered as shown in Figure 4.
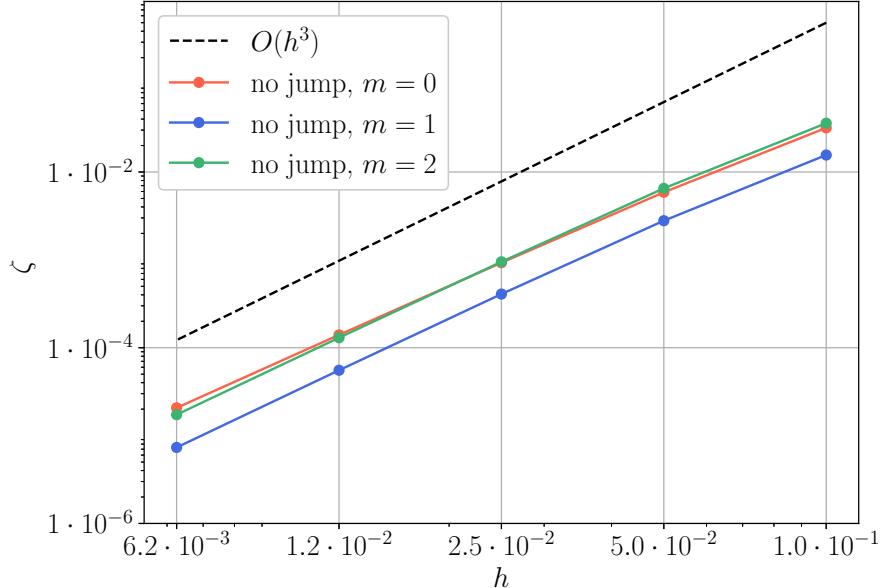

Figure 4. Order of convergence of $\mathbf{L}^2$ relative errors in magnetic field without jump in electrical current with respect to mesh size h. The dash line represents the theoretical order of convergence h^3.

Table 3. Relative errors in $\mathbf{L}^2$-norm of $\mathbf{H}$ without jump in electric potential. The mesh size is denoted by h and the number of degrees of freedom per scalar unknown by n_{dof}.

h	n_{dof}	$m = 0$	$m = 1$	$m = 2$
0.1	322	$3.18 \cdot 10^{-2}$	$1.56 \cdot 10^{-2}$	$3.59 \cdot 10^{-2}$
0.05	1034	$5.88 \cdot 10^{-3}$	$2.79 \cdot 10^{-3}$	$6.51 \cdot 10^{-3}$
0.025	3886	$9.27 \cdot 10^{-4}$	$4.08 \cdot 10^{-4}$	$9.50 \cdot 10^{-4}$
0.0125	15098	$1.40 \cdot 10^{-4}$	$5.54 \cdot 10^{-5}$	$1.30 \cdot 10^{-4}$
0.00625	59746	$2.07 \cdot 10^{-5}$	$7.33 \cdot 10^{-6}$	$1.73 \cdot 10^{-5}$

3.3.2. *Test 2: jump in $(\frac{\nabla \times \mathbf{H}}{\sigma}) \times \mathbf{n}$*

In this section, we now consider setups with a given jump of the tangential components of the electrical current across the interface Σ that either involve the Fourier mode $m = 0$, $m = 1$ or $m = 2$. We consider the same manufactured solutions $\mathbf{H}$ used in the previous section so that the jump in $\mathbf{j}$ across Σ only depends on the difference of conductivities σ_1 and σ_2 that we set to 10^4 and 1, respectively. Thus, we have:

$$\left(\frac{\nabla \times \mathbf{H}}{\sigma}\right)_{\text{jump}} = \left(\frac{1}{\sigma_1} - \frac{1}{\sigma_2}\right) \nabla \times \mathbf{H}.$$
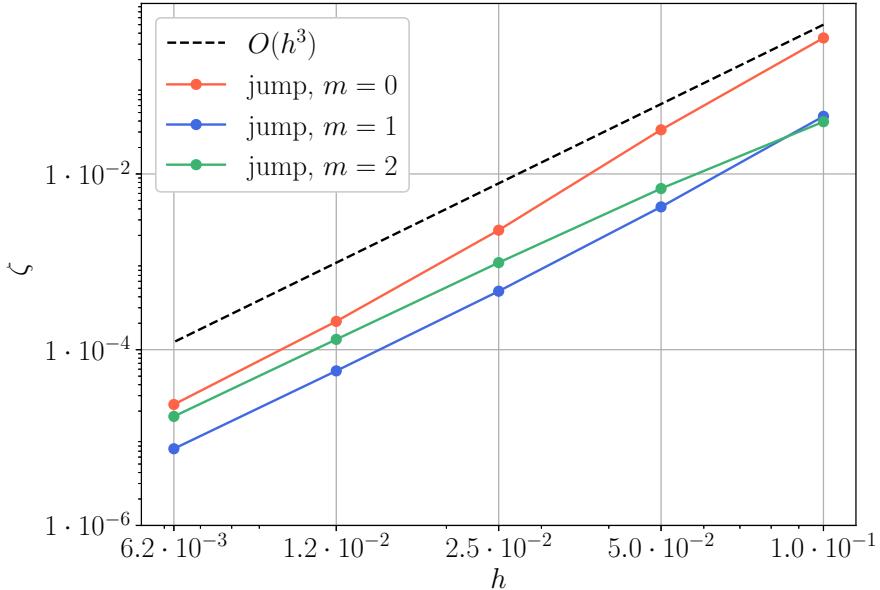

Figure 5. Order of convergence of $\mathbf{L}^2$ relative errors in magnetic field with jump in electrical current with respect to mesh size h. The dash line represents the theoretical order of convergence h^3.

We perform three sets of tests on five uniform grids. The first set of tests uses the Fourier mode $m = 0$ and the root κ_{01}, the second uses the Fourier mode $m = 1$ and the root κ_{11} while the third set uses the Fourier mode $m = 2$ and the root κ_{21}. The relative errors with respect to the mesh size are displayed in Table 4. The theoretical order of convergence, equal to three, is recovered when h tends to zero as shown in Figure 5.

Table 4. Relative errors in $\mathbf{L}^2$-norm of $\mathbf{H}$ with jump in electrical current. The mesh size is denoted by h and the number of degrees of freedom per scalar unknown by n_{dof}.

h	n_{dof}	$m = 0$	$m = 1$	$m = 2$
0.1	322	$3.53 \cdot 10^{-1}$	$4.53 \cdot 10^{-2}$	$3.93 \cdot 10^{-2}$
0.05	1034	$3.18 \cdot 10^{-2}$	$4.22 \cdot 10^{-3}$	$6.82 \cdot 10^{-3}$
0.025	3886	$2.29 \cdot 10^{-3}$	$4.63 \cdot 10^{-4}$	$9.79 \cdot 10^{-4}$
0.0125	15098	$2.10 \cdot 10^{-4}$	$5.74 \cdot 10^{-5}$	$1.31 \cdot 10^{-4}$
0.00625	59746	$2.38 \cdot 10^{-5}$	$7.46 \cdot 10^{-6}$	$1.74 \cdot 10^{-5}$

4. Numerical comparisons between models

In this section, we show that both of our formulations are indeed equivalent on setups involving continuous or discontinuous electric potential. We recall that the electric current obtained from both formulations should converge to the same current. Thus, we introduce the errors in electrical current ζ_φ and $\zeta_\mathbf{H}$ defined by:

$$\zeta_\varphi = \frac{\left\| \boldsymbol{j}_\varphi - \boldsymbol{j} \right\|}{\| \boldsymbol{j} \|}, \quad \zeta_\mathbf{H} = \frac{\left\| \boldsymbol{j}_\mathbf{H} - \boldsymbol{j} \right\|}{\| \boldsymbol{j} \|},$$

where $\|.\|$ is the L^2 norm, $\mathbf{j}$ the analytic electrical current, $\mathbf{j}_\varphi$ the current obtained with the formulation in φ, $\mathbf{j}_\mathbf{H}$ the current obtained with the formulation in $\mathbf{H}$. Three setups are considered. The first and second setups use manufactured solutions with continuous and discontinuous electric potential, respectively. Eventually, we compare both formulations on a liquid metal battery configuration.

4.1. *Setup with continuous electric potential and $\sigma = 1$*

We first compare both formulations on a setup without jump in electric potential, meaning there is also no jump in electrical current across the interface Σ. The domain Ω, and interface Σ, are defined as in Section 2.4. The electrical conductivity σ is set to one. Using the method of separation of variables, we construct the following electric potential φ and magnetic field $\mathbf{H}$:

$$\varphi(r, \theta, z) = J_m(kr) e^{im\theta} e^{kz}, \tag{12}$$

$$\mathbf{H} = -\frac{\sigma}{2} e^{kz} \begin{vmatrix} -\left(J_{m+1}(kr) + J_{m-1}(kr)\right) \sin(m\theta) \\ \left(J_{m+1}(kr) - J_{m-1}(kr)\right) \cos(mx\theta) \\ 0 \end{vmatrix} \tag{13}$$

that satisfy the relations:

$$\nabla \times \mathbf{H} = -\sigma \nabla \varphi, \qquad \nabla \cdot \mathbf{H} = 0.$$

Thus φ and $\mathbf{H}$ are solution of the problem (1) and (6), respectively. We apply Dirichlet boundary conditions for the problem in $\mathbf{H}$ on all boundaries. For the problem in φ, Dirichlet boundary conditions are applied on the lids and Neumann boundary conditions on the lateral face. To compare both formulations, we consider two setups. The first setup uses the Fourier mode $m = 0$ and the root $k = \kappa'_{01}/R$, the second one uses the Fourier mode $m = 1$ and the root $k = \kappa'_{11}/R$, while the third setup uses the Fourier mode $m = 2$ and the root $k = \kappa'_{21}/R$. We run five simulations with respective mesh size h ranging from 0.1 to 0.00625. We display the relative errors in the electrical current in Table 5 for the mode $m = 0$, in Table 6 for the mode $m = 1$ and in Table 7 for the mode $m = 2$. They show that the theoretical order of convergence, equal to two, is recovered. Thus, both methods generate an electrical current that converges to the same limit.

Table 5. Continuous electric potential with $\sigma = 1$ and $m = 0$. Order of convergence and relative errors in electrical current between both formulations in $\mathbf{H}$ and φ. Mesh size is denoted by h and the number of degrees of freedom per scalar unknown by n_{dof}.

$\mathbf{L}^2$-norm of error		Case $m = 0$		Case $m = 0$	
h	n_{dof}	Error ζ_φ	Rate	Error $\zeta_{\mathbf{H}}$	Rate
0.1	322	$1.34 \cdot 10^{-2}$	-	$1.02 \cdot 10^{-2}$	-
0.05	1034	$4.37 \cdot 10^{-3}$	1.62	$7.53 \cdot 10^{-3}$	2.30
0.025	3886	$1.22 \cdot 10^{-3}$	1.84	$1.55 \cdot 10^{-3}$	2.28
0.0125	15098	$3.07 \cdot 10^{-4}$	1.99	$3.70 \cdot 10^{-4}$	2.07
0.00625	59746	$7.72 \cdot 10^{-5}$	1.99	$9.14 \cdot 10^{-5}$	2.01

Table 6. Continuous electric potential with $\sigma = 1$ and $m = 1$. Order of convergence and relative errors in electrical current between both formulations in $\mathbf{H}$ and φ. Mesh size is denoted by h and the number of degrees of freedom per scalar unknown by n_{dof}.

$\mathbf{L}^2$-norm of error		Case $m = 1$		Case $m = 1$	
h	n_{dof}	Error ζ_φ	Rate	Error $\zeta_{\mathbf{H}}$	Rate
0.1	322	$3.50 \cdot 10^{-3}$	-	$6.70 \cdot 10^{-3}$	-
0.05	1034	$9.52 \cdot 10^{-4}$	1.88	$1.61 \cdot 10^{-3}$	2.06
0.025	3886	$2.48 \cdot 10^{-4}$	1.94	$3.80 \cdot 10^{-4}$	2.08
0.0125	15098	$6.29 \cdot 10^{-5}$	1.98	$9.34 \cdot 10^{-5}$	2.02
0.00625	59746	$1.57 \cdot 10^{-5}$	2.00	$2.27 \cdot 10^{-5}$	2.04

Table 7. Continuous electric potential with $\sigma = 1$ and $m = 2$. Order of convergence and relative errors in electrical current between both formulations in $\mathbf{H}$ and φ. Mesh size is denoted by h and the number of degrees of freedom per scalar unknown by n_{dof}.

$\mathbf{L}^2$-norm of error		Case $m = 2$		Case $m = 2$	
h	n_{dof}	Error ζ_φ	Rate	Error $\zeta_{\mathbf{H}}$	Rate
0.1	322	$6.42 \cdot 10^{-3}$	-	$1.47 \cdot 10^{-2}$	-
0.05	1034	$1.88 \cdot 10^{-3}$	1.77	$3.41 \cdot 10^{-3}$	2.11
0.025	3886	$5.41 \cdot 10^{-4}$	1.80	$7.94 \cdot 10^{-4}$	2.10
0.0125	15098	$1.37 \cdot 10^{-4}$	1.98	$1.97 \cdot 10^{-4}$	2.01
0.00625	59746	$3.46 \cdot 10^{-5}$	1.99	$4.91 \cdot 10^{-5}$	2.00

4.2. *Setup with jump in electric potential*

Our second test focuses on a setup with jump in electric potential. The domain is defined as in the previous test cases, see section 2.4, and the electrical conductivities (σ_1, σ_2) are set to $(10^4, 1)$. Using the method of separation of variables, we construct solutions for both formulations that are defined as follows:

$$\begin{cases} \varphi_1(r,\theta,z) = J_m(kr)e^{im\theta}e^{kz}, \\ \varphi_2(r,\theta,z) = \dfrac{\sigma_1}{\sigma_2}J_m(kr)e^{im\theta}e^{kz}, \end{cases} \tag{14}$$

$$\mathbf{H} = -\frac{\sigma_1}{2}e^{kz}\begin{vmatrix} -\big(J_{m+1}(kr) + J_{m-1}(kr)\big)\sin(m\theta) \\ \big(J_{m+1}(kr) - J_{m-1}(kr)\big)\cos(m\theta) \\ 0 \end{vmatrix} \tag{15}$$

where the jump in electric potential across the interface is defined by:

$$\varphi_{\text{jump}} = \left(1 - \frac{\sigma_1}{\sigma_2}\right) J_m(kr) e^{im\theta} e^{kH} \quad \text{on } \Sigma. \tag{16}$$

Table 8. Discontinuous electric potential with $(\sigma_1, \sigma_2) = (10^4, 1)$ and $m = 0$. Order of convergence and relative errors in electrical current between both formulations in $\mathbf{H}$ and φ. Mesh size is denoted by h and the number of degrees of freedom per scalar unknown by n_{dof}.

$\mathbf{L}^2$-norm of error		Case $m = 0$		Case $m = 0$	
h	n_{dof}	Error ζ_φ	Rate	Error $\zeta_{\mathbf{H}}$	Rate
0.1	322	$1.34 \cdot 10^{-2}$	-	$3.72 \cdot 10^{-2}$	-
0.05	1034	$4.37 \cdot 10^{-3}$	1.62	$7.54 \cdot 10^{-3}$	2.30
0.025	3886	$1.22 \cdot 10^{-3}$	1.84	$1.55 \cdot 10^{-3}$	2.28
0.0125	15098	$3.07 \cdot 10^{-4}$	1.99	$3.70 \cdot 10^{-4}$	2.06
0.00625	59746	$7.72 \cdot 10^{-5}$	1.99	$9.14 \cdot 10^{-5}$	2.02

We note that the electrical current $-\sigma\nabla\varphi$ is continuous across the interface Σ. Similarly, the magnetic field $\mathbf{H}$ is also continuous across Σ and the quantity $\frac{\nabla \times \mathbf{H}}{\sigma}$ satisfies

$$\left(\frac{\nabla \times \mathbf{H}_1}{\sigma_1} - \frac{\nabla \times \mathbf{H}_2}{\sigma_2}\right) \times \boldsymbol{e}_z = -\nabla(\varphi_1 - \varphi_2) \times \boldsymbol{e}_z = \left(\frac{\nabla \times \mathbf{H}}{\sigma}\right)_{\text{jump}} \times \boldsymbol{e}_z \quad \text{on } \Sigma.$$

Table 9. Discontinuous electric potential with $(\sigma_1, \sigma_2) = (10^4, 1)$ and $m = 1$. Order of convergence and relative errors in electrical current between both formulations in $\mathbf{H}$ and φ. Mesh size is denoted by h and the number of degrees of freedom per scalar unknown by n_{dof}.

$\mathbf{L}^2$-norm of error		Case $m = 1$		Case $m = 1$	
h	n_{dof}	Error ζ_φ	Rate	Error $\zeta_{\mathbf{H}}$	Rate
0.1	322	$3.52 \cdot 10^{-3}$	-	$1.63 \cdot 10^{-2}$	-
0.05	1034	$9.53 \cdot 10^{-4}$	1.89	$2.62 \cdot 10^{-3}$	2.64
0.025	3886	$2.48 \cdot 10^{-4}$	1.94	$3.40 \cdot 10^{-4}$	2.95
0.0125	15098	$6.28 \cdot 10^{-5}$	1.98	$6.97 \cdot 10^{-5}$	2.29
0.00625	59746	$1.57 \cdot 10^{-5}$	2.00	$1.70 \cdot 10^{-5}$	2.04

The boundary conditions are the same as in the previous section. We perform three sets of tests using five uniform meshes that either involve the Fourier mode $m = 0$, $m = 1$ or $m = 2$, with the respective roots $k = \kappa'_{01}/R$, $k = \kappa'_{11}/R$ or $k = \kappa'_{21}/R$. The results are displayed in Tables 8, 9 and 10. As for the case without jump, we recover the theoretical order of convergence which shows that both formulations are indeed equivalent.

We show in Figure 6 results obtained with the test $m = 0$ and a jump in electrical potential. On this figure are represented the magnetic field, the current density for both formulations and the electrical potential. We remark that the current density field is identical for both formulations. The electrical potential presents indeed a jump at the interface, whereas the magnetic field is continuous.

Table 10. Discontinuous electric potential with $(\sigma_1, \sigma_2) = (10^4, 1)$ and $m = 2$. Order of convergence and relative errors in electrical current between both formulations in $\mathbf{H}$ and φ. Mesh size is denoted by h and the number of degrees of freedom per scalar unknown by n_{dof}.

$\mathbf{L}^2$-norm of error		Case $m = 2$		Case $m = 2$	
h	n_{dof}	Error ζ_φ	Rate	Error $\zeta_{\mathbf{H}}$	Rate
0.1	322	$6.43 \cdot 10^{-3}$	-	$2.14 \cdot 10^{-2}$	-
0.05	1034	$1.88 \cdot 10^{-3}$	1.77	$3.88 \cdot 10^{-3}$	2.46
0.025	3886	$5.41 \cdot 10^{-4}$	1.80	$7.79 \cdot 10^{-4}$	2.31
0.0125	15098	$1.37 \cdot 10^{-4}$	1.98	$1.88 \cdot 10^{-4}$	2.05
0.00625	59746	$3.46 \cdot 10^{-5}$	1.99	$4.69 \cdot 10^{-5}$	2.00
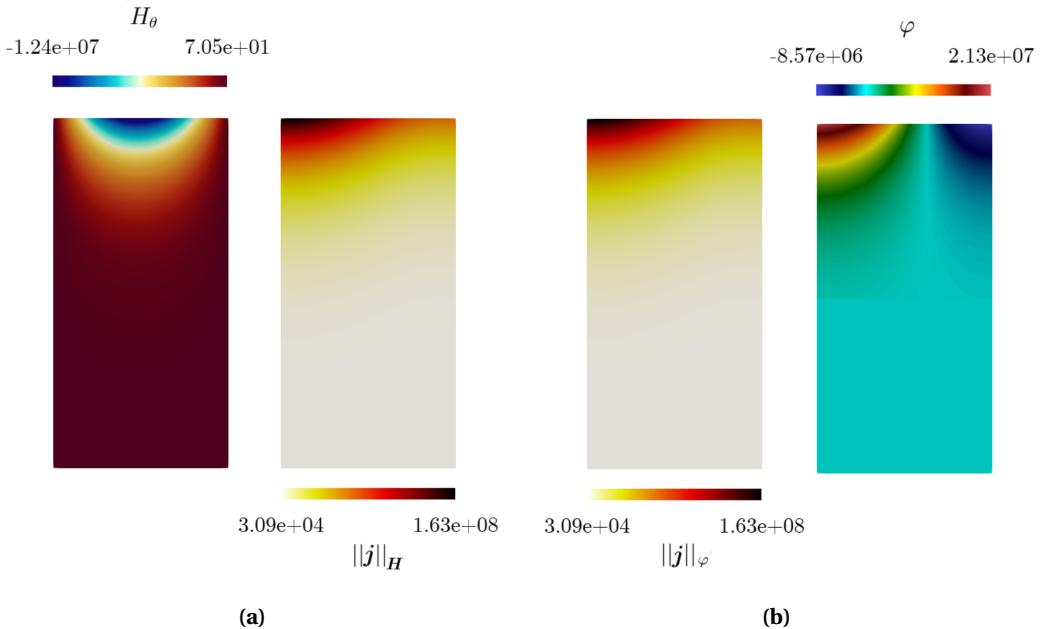
Figure 6. Snapshots of fields obtained with both formulations in non-dimensionalised units. (a) Formulation in $\mathbf{H}$, left: magnetic field H_θ and right: current density. (b) Formulation in φ, left: current density and right: electrical potential φ.

4.3. *Liquid Metal Batteries (LMB)*

In this section, we extend the comparison of our two formulations to a LMB setup. The scheme which indicates the dimensions of the setup used is shown on Figure 7a. The computations use a mesh where the mesh size h is about $R/120$. In this setup, the two liquid metals are lithium and lead. The lithium is contained in a foam (porous steel) and constitutes the negative top electrode, which is considered as solid in the simulations. The lead (alloying with lithium) constitutes the positive bottom electrode and is separated by an electrolyte. The battery is connected to the electrical circuit by two copper current collectors. The conductivities of the current collectors, the foam, the electrolyte, and the alloy are respectively:

$$\sigma_{\mathrm{Cu}} = 5.8 \cdot 10^7 \, \mathrm{S\,m}^{-1}, \sigma_{\mathrm{f}} = 2.7 \cdot 10^6 \, \mathrm{S\,m}^{-1}, \sigma_{\mathrm{e}} = 1.87 \cdot 10^2 \, \mathrm{S\,m}^{-1}, \sigma_{\mathrm{alloy}} = 7.39 \cdot 10^5 \, \mathrm{S\,m}^{-1}, \quad (17)$$

(see [22] for the material properties and the way we determine them).

We fix the incoming current I at 1 A and $\mu = \mu_0 = 4\pi\,10^{-7}\,\mathrm{kg\,m\,A^{-2}\,s^{-2}}$ the vacuum magnetic permeability everywhere. We do not solve the velocity and the concentration fields in these simulations.

The boundary conditions for the potential are:

$$-\sigma_{\mathrm{Cu}}\partial_z\varphi|_{z=H_b+H+H_{\mathrm{el}}+H_f+H_w} = \frac{JR^2}{R_w^2}, \qquad \partial_n\varphi|_{r\geq R_w,z>0} = 0, \qquad \varphi|_{z=0} = 0 \qquad (18)$$

and the ones for the magnetic field are:

$$H_\theta|_{z=H_b+H+H_{\mathrm{el}}+H_f+H_w} = \frac{J}{2}\frac{R^2}{R_w^2}r, \qquad H_\theta|_{r\geq R_w,z>0} = \frac{J}{2}\frac{R^2}{r}, \qquad (\nabla\times \boldsymbol{H})\times\boldsymbol{n}|_{z=0} = \boldsymbol{0} \qquad (19)$$

where J is the fixed current density in the alloy, such that $J = I/(\pi R^2)$. We note that the above boundary conditions are equivalent so we can compare the electrical current produced with both formulations.

We first study a simple case where the jump in potential is constant, $\varphi_{\mathrm{jump}} = -0.8$ V. This is equivalent to $(\frac{\nabla\times\boldsymbol{H}}{\sigma})_{\mathrm{jump}} = \boldsymbol{0}$. We show the results in Figure 8. The first panel (8a) shows a snapshot of the electrical potential obtained with the potential formulation. We notice the constant jump of (-0.8) V at the electrolyte-alloy interface that we can also observe on Figure 8b, where we plot the electrical potential as a function of z at different r. The profile along the z-axis is coherent with the profile obtained by [8] with a Li-Bi battery. Figure 8c shows the streamlines of the electrical current obtained using both formulations and colored by the amplitude of j_z. This figure shows that the current is identical in both cases.
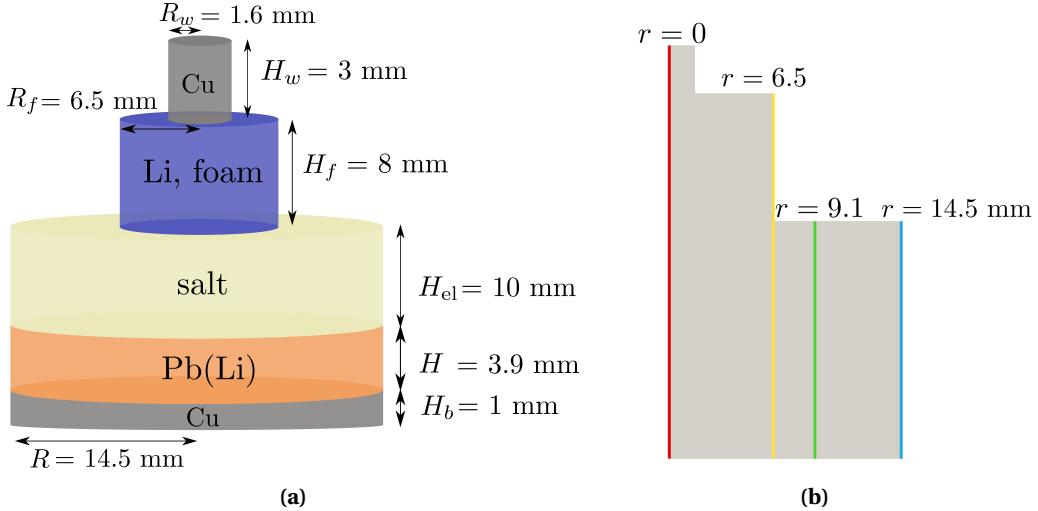

Figure 7. (a) Scheme of the LMB setup used for the comparison between both simulations. (b) Scheme of a meridian plane of the prototype. Because the following simulations are axisymmetric, the snapshots are represented on such a meridian plane. The colored lines represent the profiles used for Figures 8b and 9b.

We then study a case where the jump in potential is a function of r, $\varphi_{\mathrm{jump}} = -J_0(kr)$ (in V), where $k = \kappa'_{01}/R$. This is equivalent to $\left(\frac{\nabla\times\boldsymbol{H}}{\sigma}\right)_{\mathrm{jump}} = kJ'_0(kr)\boldsymbol{e}_r$. We show the results on Figure 9. On Figure 9a we show a snapshot of the electrical potential obtained with the potential formulation. We notice that the jump at the electrolyte-alloy interface varies with r. This can also be observed on Figure 9b where we plot the electrical potential as a function of z at different r. Figure 9c shows the streamlines of the electrical current obtained using both formulations and colored by
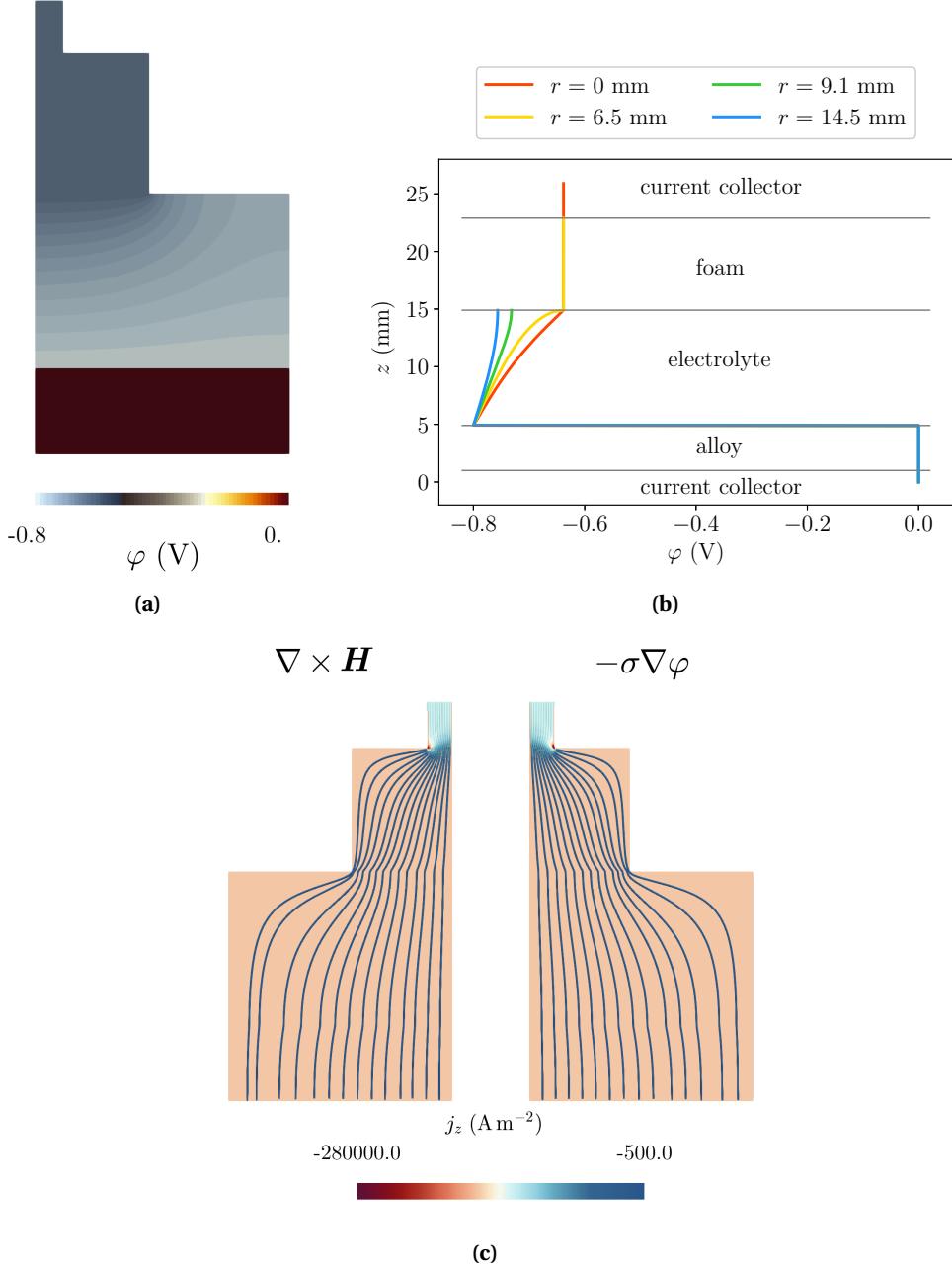
Figure 8. Case with a jump in electrical potential φ_{jump} = -0.8 V. (a) Snapshot of the electrical potential (in V). (b) Profile of the electrical potential as a function of z at different r. (c) Streamlines of the current density colored with amplitude of j_z (in A m^{-2}) in a meridian plane, in both cases: (left) problem with **H**, (right) problem with φ.

the amplitude of j_z. This figure shows that the current is identical in both cases. We note that the current loop appears due to the form of the jump in potential that now depends on the position r on the interface Σ.

(a)

(b)

(c)
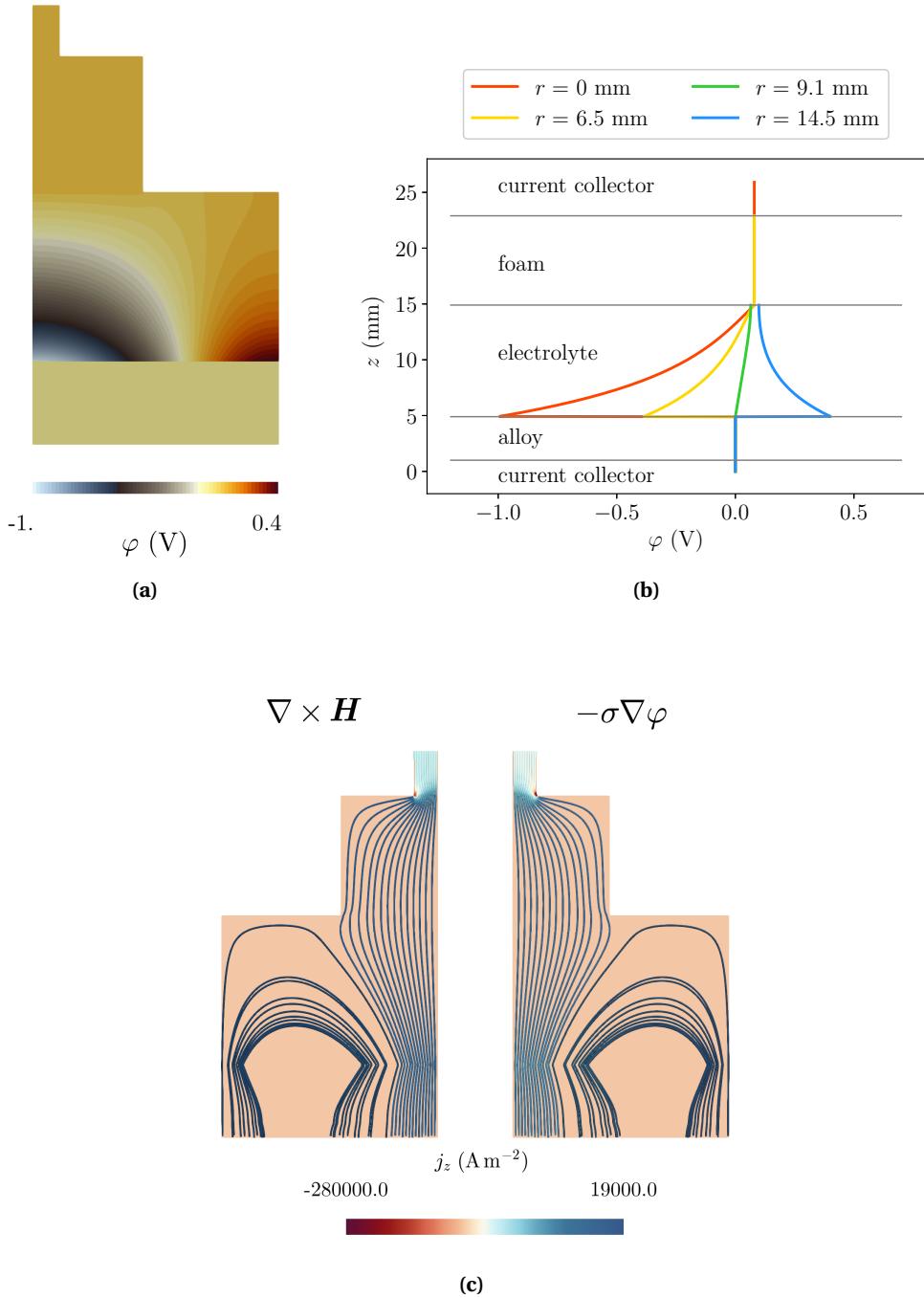
Figure 9. Case with a jump in electrical potential φ_{jump} = - $J_0(kr)$ (in V). (a) Snapshot of the electrical potential (in V). (b) Profile of the electrical potential as a function of z at different r. (c) Streamlines of the current density colored with amplitude of j_z (in A m^{-2}) in a meridian plane, in both cases: (left) problem with **H**, (right) problem with φ.

5. Conclusion

In this article, we have proposed a new formulation of discontinuous electrical potential distributions based on the magnetic field. We have first presented a formulation of these distributions based on the electrical potential as is done in a FVM approach [8, 9, 12]. We have written a corresponding FEM numerical code that we have validated in a cylindrical domain, considering continuous and discontinuous distributions of electrical potential. We have then introduced a new magnetic field based formulation, and theoretically showed the equivalence between both approaches. We have developed a FEM numerical code with this magnetic formulation and validated it in the same manner as the electrical potential one. Finally, we have shown that both numerical solutions are equivalent in the cylindrical domain considered as well as in a LMB setup.

It is now recognized that mass transport plays a key role in the LMB efficiency by influencing the concentration distribution in the bottom electrode [23]. The local concentration of ions at the electrolyte-electrode interface determines the jump in electrical potential (through a Nernst equation) that impacts the current distribution. This current is related to the incoming flux of ions, therefore to the concentration. These couplings are crucial for determining the concentration of ions in the electrode bulk where inhomogeneity leading to the formation of intermetallics is to be avoided. A future extension to the present work is the application of the magnetic field based formulation on a LMB setup coupled with the concentration and the velocity fields, in order to examine the impact of an electrical potential jump on the concentration distribution in the bottom electrode.

Conflicts of interest

The authors declare no competing financial interest.

Dedication

The manuscript was written through contributions of all authors. All authors have given approval to the final version of the manuscript.

Acknowledgments

References

[1] M. O. Bristeau, R. Glowinski, J. Periaux, "Numerical methods for the Navier–Stokes equations. Applications to the simulation of compressible and incompressible viscous flows", *Comput. Phys. Rep.* **6** (1987), no. 1-6, p. 73-187.

[2] R. Glowinski, P. Le Tallec, *Augmented Lagrangian and operator-splitting methods in nonlinear mechanics*, SIAM Studies in Applied Mathematics, vol. 9, Society for Industrial and Applied Mathematics, 1989.

[3] R. Glowinski, "Finite element methods for incompressible viscous flow", in *Numerical methods for fluids (Part 3)*, Handbook of Numerical Analysis, vol. 9, Elsevier, 2003, p. 3-1176.

[4] R. Glowinski, S. J. Osher, W. Yin, *Splitting methods in communication, imaging, science, and engineering*, Scientific Computation, Springer, 2017.

[5] R. Glowinski, *Lectures on numerical methods for non-linear variational problems*, Springer, 2008.

[6] J.-L. Guermond, P. Minev, J. Shen, "An overview of projection methods for incompressible flows", *Comput. Methods Appl. Mech. Eng.* **195** (2006), no. 44-47, p. 6011-6045.

[7] H. Kim, D. A. Boysen, J. M. Newhouse, B. L. Spatocco, B. Chung, P. J. Burke, D. J. Bradwell, K. Jiang, A. A. Tomaszowska, K. Wang, W. Wei, L. A. Ortiz, S. A. Barriga, S. M. Poizeau, D. R. Sadoway, "Liquid Metal Batteries: Past, Present, and Future", *Chem. Rev.* **113** (2013), no. 3, p. 2075-2099.

[8] N. Weber, S. Landgraf, K. Mushtaq, M. Nimtz, P. Personnettaz, T. Weier, J. Zhao, D. R. Sadoway, "Modeling discontinuous potential distributions using the finite volume method, and application to liquid metal batteries", *Electrochim. Acta* **318** (2019), p. 857-864.

[9] C. Duczek, N. Weber, O. E. Godinez-Brizuela, T. Weier, "Simulation of potential and species distribution in a Li‖Bi liquid metal battery using coupled meshes", *Electrochim. Acta* (2022), article no. 141413.

[10] G. A. Prentice, C. W. Tobias, "A Survey of Numerical Methods and Solutions for Current Distribution Problems", *J. Electrochem. Soc.* **129** (1982), no. 1, p. 72-78.

[11] A. Z. Weber, J. Newman, "Modeling Transport in Polymer-Electrolyte Fuel Cells", *Chem. Rev.* **104** (2004), no. 10, p. 4679-4726.

[12] N. Weber, M. Nimtz, P. Personnettaz, T. Weier, D. R. Sadoway, "Numerical simulation of mass transfer enhancement in liquid metal batteries by means of electro-vortex flow", *Journal of Power Sources Advances* **1** (2020), article no. 100004.

[13] G. Guidoboni, R. Glowinski, N. Cavallini, S. Canic, "Stable loosely-coupled-type algorithm for fluid–structure interaction in blood flow", *J. Comput. Phys.* **228** (2009), no. 18, p. 6916-6937.

[14] J.-L. Guermond, R. Laguerre, J. Léorat, C. Nore, "An interior penalty Galerkin method for the MHD equations in heterogeneous domains", *J. Comput. Phys.* **221** (2007), no. 1, p. 349-369.

[15] J.-L. Guermond, R. Laguerre, J. Léorat, C. Nore, "Nonlinear magnetohydrodynamics in axisymmetric heterogeneous domains using a Fourier/Finite Element technique and an Interior Penalty Method", *J. Comput. Phys.* **228** (2009), no. 8, p. 2739-2757.

[16] J.-L. Guermond, J. Léorat, F. Luddens, C. Nore, A. Ribeiro, "Effects of discontinuous magnetic permeability on magnetodynamic problems", *J. Comput. Phys.* **230** (2011), no. 16, p. 6299-6319.

[17] A. Ern, A. F. Stephansen, P. Zunino, "A discontinuous Galerkin method with weighted averages for advection–diffusion equations with locally small and anisotropic diffusivity", *IMA J. Numer. Anal.* **29** (2009), no. 2, p. 235-256.

[18] M. Costabel, "A coercive bilinear form for Maxwell's equations", *J. Math. Anal. Appl.* **157** (1991), no. 2, p. 527-541.

[19] A. Bonito, J.-L. Guermond, "Approximation of the eigenvalue problem for the time harmonic Maxwell system by continuous Lagrange finite elements", *Math. Comput.* **80** (2011), no. 276, p. 1887-1910.

[20] A. Bonito, J.-L. Guermond, F. Luddens, "An interior penalty method with C0 finite elements for the approximation of the Maxwell equations in heterogeneous media: convergence analysis with minimal regularity", *ESAIM, Math. Model. Numer. Anal.* **50** (2016), no. 5, p. 1457-1489.

[21] A. Bonito, J.-L. Guermond, F. Luddens, "Regularity of the Maxwell equations in heterogeneous media and Lipschitz domains", *J. Math. Anal. Appl.* **408** (2013), no. 2, p. 498-512.

[22] W. Herreman, S. Bénard, C. Nore, P. Personnettaz, L. Cappanera, J.-L. Guermond, "Solutal buoyancy and electrovortex flow in liquid metal batteries", *Phys. Rev. Fluids* **5** (2020), article no. 074501.

[23] P. Personnettaz, S. Landgraf, M. Nimtz, N. Weber, T. Weier, "Mass transport induced asymmetry in charge/discharge behavior of liquid metal batteries", *Electrochem. commun.* **105** (2019), article no. 106496.